Computational optimisation of optical projection tomography for 3D image analysis

Tang, X.

Chapter 2

Fast Post-processing Pipeline for Optical Projection Tomography

This chapter is based on the following publications:

Tang X., Hoff V.M., Hoogenboom J., Guo Y., Cai.F., Lamers G. & Verbeek F. (2016), Fluorescence and bright-field 3D image fusion based on sinogram unification for optical projection tomography. In: Tian T., Jiang Q., Liu Y., Burrage K., Son J., Wang Y., Hu X., Morishita S., Zhu Q., Wang G. (Eds.) *Proceedings 2016 IEEE International Conference on Bioinformatics and Biomedicine Dec 15-18, 2016 Shenzhen, China.* Danvers: *Institute of Electrical and Electronics Engineers* (*IEEE*). 403-410.

Tang X., Zwaan D.M. van der, Zammit A., Rietveld K.F.D. & Verbeek F.J. (2017), Fast Post-Processing Pipeline for Optical Projection Tomography, *IEEE Transactions on NanoBioscience* 16(5): 367-374.

Chapter summary

In order to improve the effectiveness and efficiency of 3D reconstruction for optical projection tomography, we present a fast post-processing pipeline. This pipeline includes image cropping, background subtraction, centre of rotation correction and 3D reconstruction. For OPT imaging, with respect to the centre of rotation correction, a novel algorithm based on interest point detection in the sinogram is proposed. Instead of locating the centre of rotation on single sinogram, we intermittently and evenly select sinograms in the detected full range of a sample to make the located centre of rotation more robust. The post-processing pipeline presented is implemented on a parallel manner and experiments demonstrate that the average runtime for images of size 1036×1360×400 pixel can be less than 1 minute on a computer cluster of which 5 compute nodes are used.

2.1 Introduction

In this section we will state our research question and introduce our perspective on optical projection tomography (OPT) imaging and reconstruction framework. It includes a brief introduction of our contribution to this research as well as related work in this field of research.

2.1.1 Research problem

The aim of an OPT imaging system is to obtain a 3D volume image, so that this volume image can be used for analysis and visualization. This is accomplished by a reconstruction algorithm that is applied on the sinograms derived from the OPT image. With an OPT imaging system a so called tomogram is acquired. The tomogram is a collection of images of a specimen taken at regular angular intervals. For OPT this typically comprised a stepwise acquisition of the images over a full revolution of the sample. The tomogram is transformed to a sinogram in which all projections are represented.

The reconstruction process could, however, introduce various artefacts depending on different imaging setups. This means that for each individual OPT imaging system, exploration and elimination of reconstruction artefacts are necessary. In this chapter, we will focus on the artefacts resulting from the misalignment of centre of rotation (CoR).

Another important issue for OPT imaging system is the speed of reconstruction process. In order to be able to apply OPT in a high-throughput setting as well as to allow quick reconstruction of the imaging, research on fast and efficient reconstruction is important. These two issues represent the general motivation for the work in this chapter.

With the two research questions, we propose a fast post-processing pipeline that is integrated into reconstruction software. In this pipeline, cropping and background subtraction are the first two steps for image pre-processing, followed by a fast and efficient CoR correction and a 3D reconstruction algorithm. This significantly contributes to the innovation in our OPT applications. With the application of cropping and CoR correction, the sample can be placed at any position of the field of view (FoV), decreasing the time for post-processing of tomogram and avoiding the calibration process prior to tomogram acquisition. Originally, a calibration helps to align the CoR to the centre of FoV, which normally takes several minutes. In this pipeline, we implement a parallel computation of both CoR correction and 3D reconstruction to further accelerate the post-processing of OPT tomogram.

2.1.2 Related work

In the recent years, cancer progression [5]–[7], drug discovery [8] and development studies for organ system such as skeleton [9], [10], teeth [38] and blood vessels [12] have benefited from the further development of OPT microscopy. Kumer *et al*. [5] applied OPT to adult

zebrafish to study the synchronous development of cancer and vasculature in adult zebrafish. McGinty *et al.* [8] proposed a fluorescence lifetime optical projection tomography in 2011 for biological research and drug discovery, the time for image acquisition and post-processing including 3D reconstruction were both reported to be ~20 minutes. Later, in 2012, Fieramonti *et al.* [9] extended OPT to optically diffusive samples for studying skeletal and nervous structures in zebrafish, improving the acquisition time to something like ~3 minutes but without considering the artefacts produced when the CoR is inconsistent with the centre of the tomogram. Agarwal *et al.* [7] presented a diagnosis method of early cancer by reconstructing 3D cellular image with OPT. The high resolution of single cells was achieved by using a large NA and scanning the objective focal plan contributed to the extension of DOF, which consequently increased the light dose and acquisition time. More recent, in 2015, Correia *et al.* [12] introduced accelerated OPT by decreasing the number of rotations at tomogram acquisition, aiming to improve the efficiency of OPT system and decrease the light dose the sample is exposed to. In similar fashion, aiming at improving the efficiency of OPT imaging, we present a fast OPT post-processing pipeline which contains pre-processing, CoR correction and 3D reconstruction taking ~1 minute with tomogram size of 1036×1360×400 pixels.

Before applying the inverse radon transform to the sinogram for reconstruction, by definition the position of the CoR should be in the middle of the sinogram, achieved by CoR correction. This was first studied in 1990 [39] in computational CT. Previous studies showed that shifted CoR could introduce severe artefacts or even incorrect results [40]. Furthermore, correcting CoR based on images can bypass the calibration prior to tomogram acquisition, improving the efficiency of the imaging system. In terms of methodologies for CoR correction, there are two mainstream approaches. The first approach is based on signal match for pairs of projection data (180° opposed to each other) [39], [41]–[43]. This is widely used in CT because the intensities from two opposite projected angles are theoretically equivalent in CT imaging. Unfortunately, this method may not be directly suitable for OPT images, as opposite projected data may vary at different sample angles. The differences are caused by the fact that the lens introduces a DoF and only images the front half of the sample [44]. Moreover, feasibility is hampered as the sinogram is often disturbed by fixation artefacts and/ or random noise; both frequently occur in OPT imaging.

The second approach both for CT and OPT is based on iterative reconstruction of the sinogram [22], [45], [46]. The vertical axis that is producing the smallest variance in the reconstructed image is chosen as the CoR, cf. [46]. This approach is however time-consuming and therefore less used in CT. Furthermore, both approaches chose only one sinogram for CoR correction, whereas the CoR fluctuation produced by different sinograms was not taken into account, to some extent resulting in unconvincing CoR.

2.2 Materials and methods

An OPT system that is used for 3D imaging in biomedical research, e.g. embryo or skeleton development, requires the sample, i.e. a zebrafish larvae, first to be prepared for imaging. A clearing of the sample is accomplished with the BABB protocol, cf. § 1.2.4. The data flow of a sample goes from preparation, to OPT image acquisition using our dedicated imaging software, cf. § 1.2.3, to the production of the OPT tomogram. This tomogram is then reconstructed to 3D image by using the OPT reconstruction software which will be further elaborated in this section. The OPT reconstruction software integrates the whole reconstruction pipeline. For the CoR correction and 3D reconstruction tasks, it provides the interface to submit the tasks to our compute cluster, i.e. the Leiden Life Science Cluster (LLSC).

2.2.1 OPT imaging

Our OPT imaging system supports both bright-field and fluorescence illumination. The acquisition time for a bright-field tomogram is less than 3 minutes, and for a fluorescence tomogram it varies depending on the strength of the fluorescence and exposure time; but normally it is less than 10 minutes for a sample in a full revolution, cf. § 1.2.3. Optimisation of sample preparation protocol and image acquisition were implemented as described in chapter 1, cf. § 1.2.4. The tomogram of a single channel from the OPT is a 16-bit image of size 1036×1360×400 pixels, with a file size of 1.05GB. Image of 1036×1360 is acquired over 400 rotation angles in [0°, 360°). For each tomogram, 10 background images of the same size are acquired for the post-processing. The acquisition of the tomogram is separated from the computationally more demanding post-processing. This is accomplished on a cluster computer and communication to the cluster application is realized via a web-service that is available on the acquisition computer.

Application of the post-processing pipeline, implies that the acquired OPT tomograms will be first cropped to the region of interest (RoI). It is followed by a background subtraction of the median of the background images for each channel. Subsequently, CoR correction and 3D reconstruction are applied. The user interface of the post-processing software is shown in Figure 2.1 with an example of a zebrafish in bright-field. Cropping and background subtraction are implemented locally on the left side, and on the right we can upload the data to our computer cluster (LLSC) for CoR correction and reconstruction. Once the task is finished, the resulting 3D image will be automatically stored on the LLSC file server and a file link for downloading is returned. At the same time the reconstructed 3D image is downloaded to the local computer, cf. right panel in the user interface as shown Figure 2.1. Users can also visualize the x-projection and y-projection using the Details button. The file link for users to download the 3D image is provided under the Details button on the right of user interface.

2.2.2 OPT reconstruction software

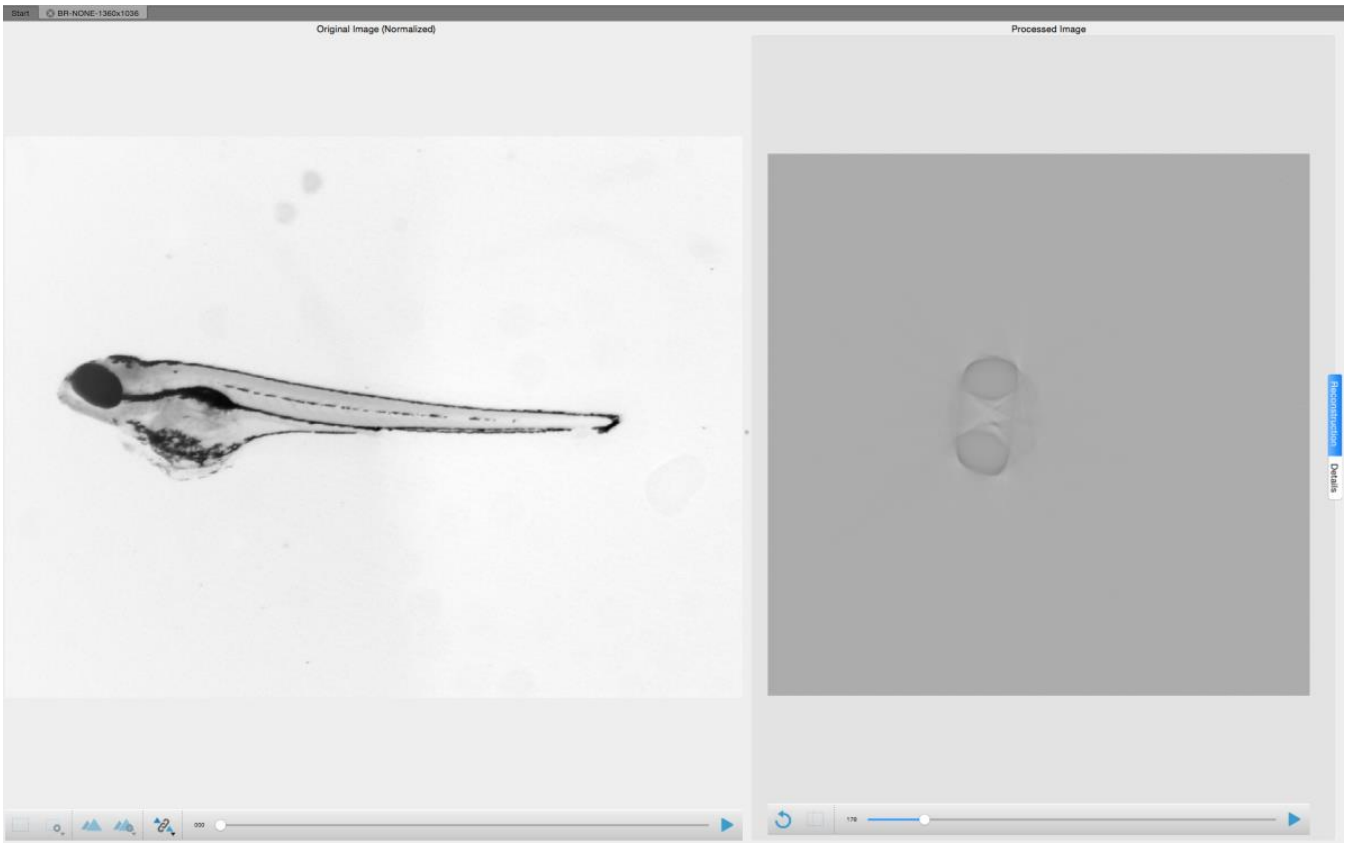

Figure 2.1. The user interface of the post-processing software; it includes cropping, background subtraction, CoR correction and 3D reconstruction. Once the tomogram is opened, cropping and background subtraction can be done with buttons on the left. With a Start Reconstruction button, the data are automatically uploaded to a dedicated cluster computer. The CoR correction and reconstruction are distributed on the cluster. The reconstructed results and maximum intensity projections are sent to the local computer after completion (right panel).

2.2.3 Cluster computing: the LLSC

The LLSC is a computer cluster for bioinformatics applications. As displayed in Figure 2.2, it consists of three user nodes, 20+ compute nodes and a file server. Each compute node consists of multiple two Intel Xeon dual- or quad-core processors with 16GB RAM, forming a cluster of 108 processors in total. The separate file server has 36TB storage. The nodes and file server are connected using Gigabit Ethernet. The LLSC currently uses the TORQUE job scheduler [47] to allocate the computational tasks, but a future upgrade to the SLURM workload Manager [48] is planned. To ensure consistent performance measurements we will be using the nodes that contain two Intel Xeon 5150 dual-core processors and two Intel Xeon e5430 dual-core processors, given that most of the currently operational nodes in the cluster are of these types.

Figure 2.2. The LLSC cluster with three user nodes, 20 computing nodes (108 processors) and a file server.

2.3 Implementation

In this section we present our specific contributions to the post-processing pipeline, i.e. the CoR correction algorithm and Reconstruction on the LLSC system.

2.3.1 CoR correction

CoR correction involves CoR localization for each of the channels and the CoR alignment of these multiple channels. Considering the artefacts from CoR shift depicted in [22], [49] and the computationally expensive problem of the traditional CoR localization method by using iterative reconstruction [46], a novel CoR localization approach is presented. The CoR localization for each channel is defined as searching for most frequently occurring value from the obtained CoRs of multiple sinograms, which are localized based on interest point detection and CoR optimisation function.

1) Sinogram selection

To make the CoR localization in each channel convincing, multiple sinograms are selected. We select these multiple sinograms by investigating the slice range *NS* from 4 valid sinogram ranges using:

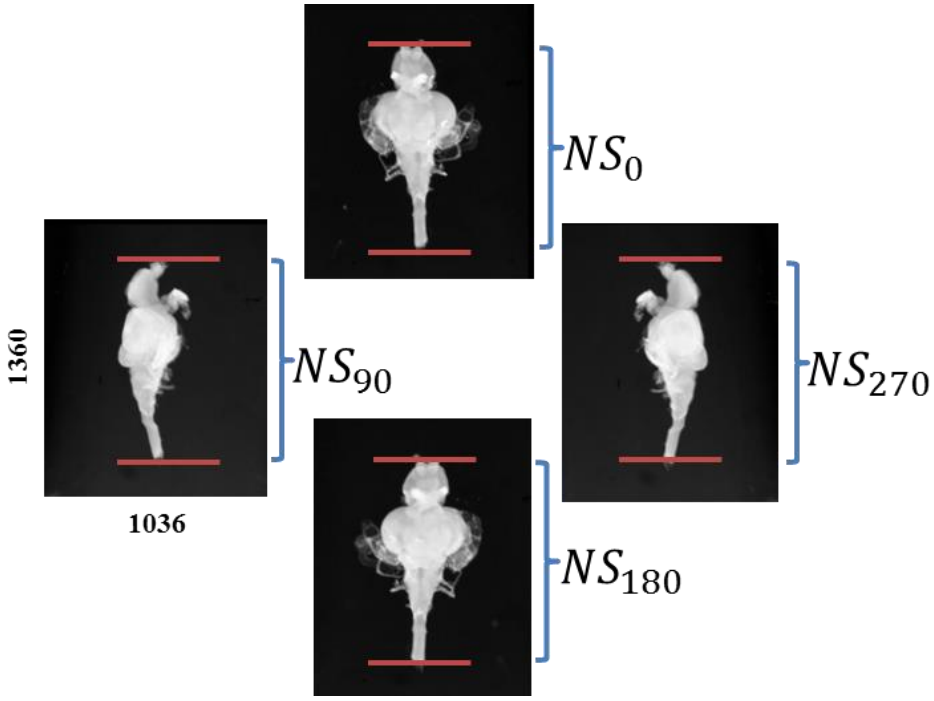

Figure 2.3. The 4 orthogonal sinogram ranges NS_0, NS_{90}, NS_{180} and NS_{270} are from the 4 orthogonal tomogram images ($0^\circ, 90^\circ, 180^\circ, 270^\circ$) of an adult zebrafish brain.

$$NS = NS_0 \cap NS_{90} \cap NS_{180} \cap NS_{270} \quad (1)$$

NS_0, NS_{90}, NS_{180} and NS_{270} respectively represent the 4 slice ranges of 4 orthogonal tomogram images of size 1360×1036, as shown in Figure 2.3. Here, as an example we look at the brain of an adult zebrafish. Within *NS*, the step for selecting a sinogram $step = ceil(\frac{NS}{\rho})$ is experimentally determined and approximately ρ sinograms from the range *NS* are evenly selected. The selected set of sinograms is defined as *S*. In this manner, specimen samples have approximately the same number of selected sinograms for CoR localization regardless of their different sizes.

2) Interest point detection

According to the design of our OPT imaging system, only the front half of the sample is in the DoF, so the projected data from opposite angles may vary differently depending on the rotation angle, specimen size and shape. However, a voxel projected at the left or right boundary of the specimen shares approximately the same image intensity with the opposite projection of the same sample location. This equivalence is shown as a peak and a trough along the sinogram. To illustrate our assumption, a sinogram from the fluorescence tomogram of a zebrafish larva is depicted as an example in Figure 2.4. Point O, A and B are the fluorescence signals of the 6 days post fertilization (*dpf*) zebrafish eye from 3 different angles, and O*, A* and B* are their corresponding opposite projections.

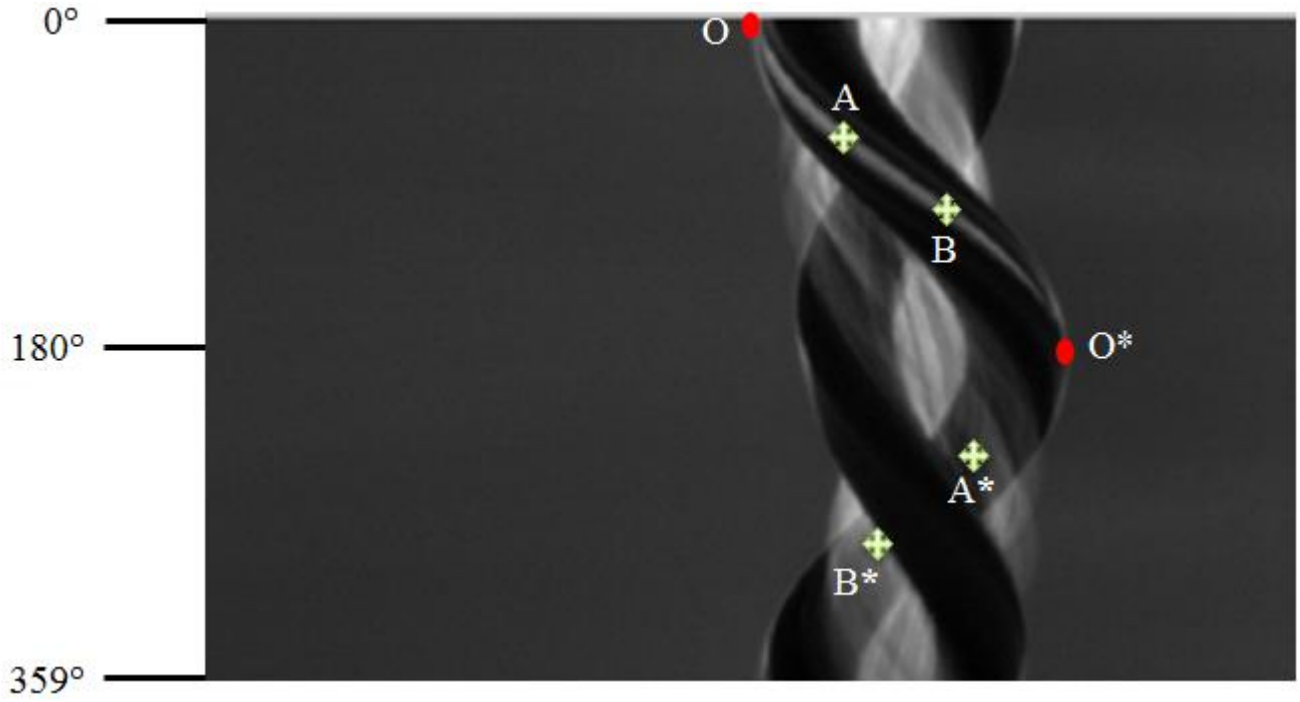

Figure 2.4. A sinogram of a zebrafish embryo showing the differences among pairs of opposite projected data. O and O*, A and A*, B and B* are pairs respectively. O and O* are interest points; while A and A*, B and B* are not.

The projected data for a voxel in the eye should be formed as a sine function passing through O, A, B, O*, A* and B* in CT system, but in OPT only O and O* remain equivalent; while A and A* as well as B and B* differ significantly, being consistent with the assumption above. With this assumption, the CoR should be located with the oppositely projected pairs that are similar to O and O*. The problem of locating the CoR is therefore transformed as search for peaks and troughs on the sinogram edge; in our case defined as interest points.

A sinogram is defined as $S(\xi, \varphi)$ where φ is the rotation angle, and ξ is the phase in each angle. The size of the sinogram is $\phi \times p$ in our case, with ϕ being the number of sample angles and p being the tomogram height after cropping. As depicted in the flowchart in Figure 2.5, the procedure for detecting interest point is based on point selection from initial points $E = \{\xi_k,\ \varphi_k\},\ \ k \in [1, M]$. E is the collection of points using edge detection in a sinogram with M being the number of initial points. $S_b(\xi, \varphi)$ refers to the binary sinogram. After point selection, the detected interest points are $P = \{\xi_j, \varphi_j\},\ \ j \in [1, N]$, and $N \leq M$. In Figure 2.5, the detailed algorithm for point selection is presented in the flowchart.

As shown in Figure 2.5, $W0_k$ and W_k are the window patches of an initial point $(\xi_{one}, \varphi_{one}) \in E$, meeting different conditions. ED_k is the image edge detected from W_k. In W_k we define θ as the angle passing through the 0-labeled centre $(\xi_{\text{zero}}, \varphi_{\text{zero}})$ and the 1-labeled centre $(\xi_{one}, \varphi_{one})$ that are separated by edge ED_k. If ED_k is enclosed, we

set a constraint of $\tan\theta < \frac{1}{3}\sqrt{3}$, where $\arctan\frac{1}{3}\sqrt{3} = 30°$, therefore only points with $\theta < 30°$ will remain. The peak and trough within W_k (indicated with red stars in Figure 2.6) are defined as follows:

$$\text{Peak:}\begin{cases} \xi_{zero} > \xi_{one} \\ |D_\varphi| = (w_1 - 1) \\ D(D_\xi) < 0 \\ 1 \notin sign(d_{\xi 1}) \\ 1 \notin sign(d_{\xi 2}) \end{cases} \qquad \text{Trough:}\begin{cases} \xi_{zero} < \xi_{one} \\ |D_\varphi| = (w_1 - 1) \\ D(D_\xi) > 0 \\ -1 \notin sign(d_{\xi 1}) \\ -1 \notin sign(d_{\xi 2}) \end{cases} \tag{2}$$

D_φ symbolizes the sum of derivatives of ED_k in the φ direction along the edge curve, while $D(D_\xi)$ is the sum of second derivatives of ED_k in the ξ direction along the edge curve. When $D(D_\xi) < 0$, the function of the ED_k sequence is constrained as being convex, and if $D(D_\xi) > 0$, it is concave, corresponding to the peak and trough, respectively. We break ED_k into upper and lower edges: ED_{k1} and ED_{k2}, both of which are started at the middle of ED_k in the φ direction. Now, $d_{\xi 1}$ and $d_{\xi 2}$ are separately the derivatives of ED_{k1} and ED_{k2} in the ξ direction.

Applying the definition from Eq. (2), false-peak and false-trough (indicated with purple stars in Figure 2.6) are not kept as interest points, as they are not true sine peaks but rather intersections of different sine functions, which should therefore be discarded. Furthermore, when a true trough satisfies *R* (yellow star in Figure 2.6),

$$R = \begin{cases} \xi_{zero} < \xi_{one} \\ |D_\varphi| = (w_1 - 1) \\ D(D_\xi) = 0 \\ sign(d_{\xi 1}) = 0 \\ sign(d_{\xi 2}) = 0 \end{cases} \tag{3}$$

or a true peak satisfies *Q*,

$$Q = \begin{cases} \xi_{zero} > \xi_{one} \\ |D_\varphi| = (w_1 - 1) \\ D(D_\xi) = 0 \\ sign(d_{\xi 1}) = 0 \\ sign(d_{\xi 2}) = 0 \end{cases} \tag{4}$$

The edge ED_k in W_k of size w_1 is strictly vertical. Then it does not satisfy the definition of peak or trough in Eq. (2). The reason for the inconsistency is caused by the size of W_k. Therefore, to solve this problem, a bigger patch (set as $2w_1$+1 in our experiment) is set to satisfy Eq. (2) in a bigger patch, following the same steps for interest point detection in Figure 2.5.

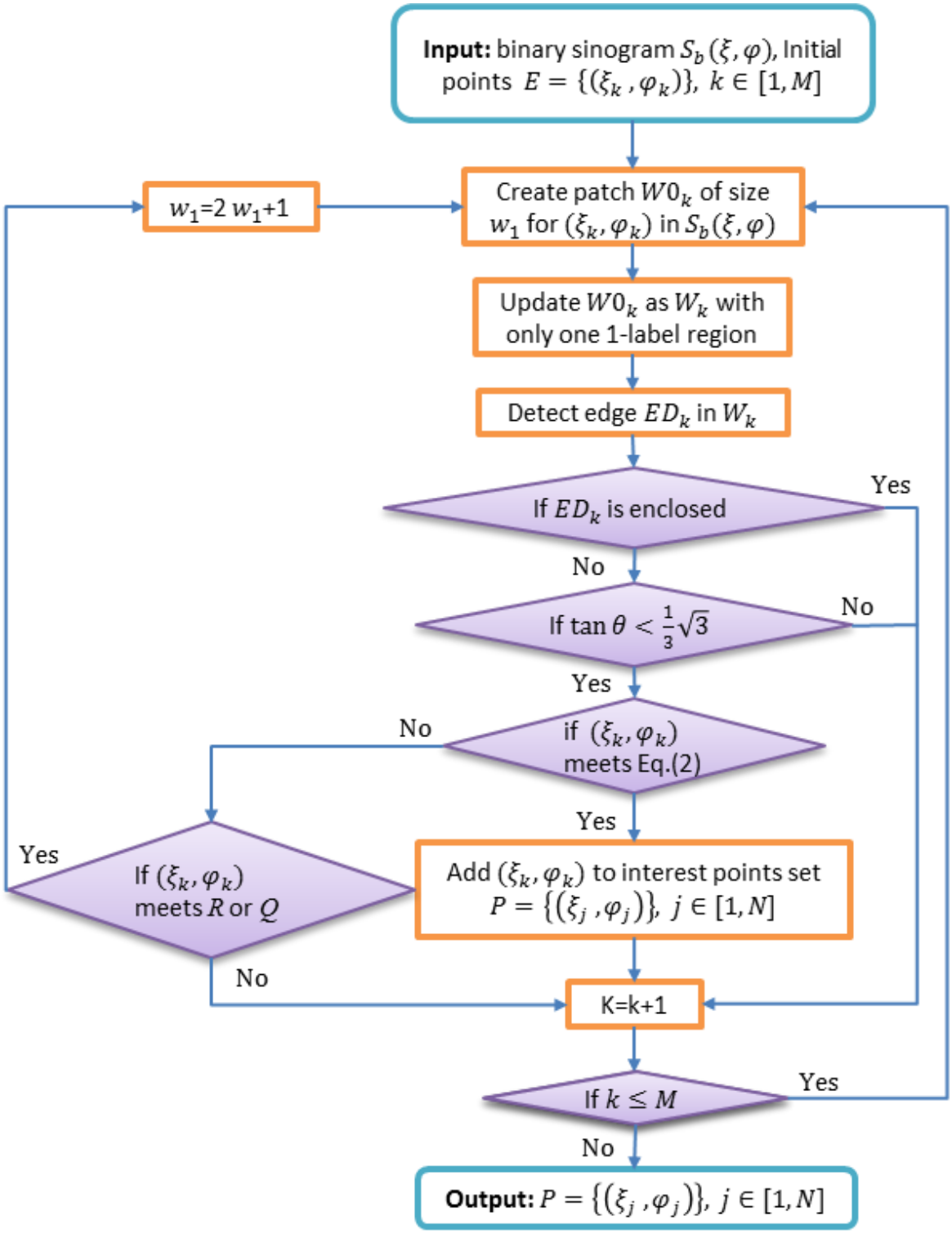

Figure 2.5. Flowchart of the algorithm for interest point detection. The binary sinogram and initial points are obtained through OSTU segmentation [50] and the Sobel edge detector [51] respectively.

3) CoR localization and alignment

According to the definition of CoR localization above, CoR for single sinogram should be first localized. With the interest points $P = \{\xi_j, \varphi_j\}$, $j \in [1, N]$ detected in single sinogram, the CoR range is obtained as $[\xi_{min}, \xi_{max}]$, where ξ_{max} and ξ_{min} are respectively the maximum and minimum of ξ_j in the interest points P. For a specific CoR value c, we locate the corresponding opposite points for P as $P_c' = \{(\xi_j, \varphi_j)_c'\}$, $j \in [1, N]$, which are symmetric by c and have an interval of π in projection. To find a mathematical metric between P and P_c', we define the neighbors of (ξ_j, φ_j) and $(\xi_j, \varphi_j)_c'$ as $r_c(\xi_j, \varphi_j)$ and $r_c'(\xi_j, \varphi_j)$. As shown in Figure 2.4, the projection data between interest point (ξ_j, φ_j) and its opposite point $(\xi_j, \varphi_j)_c'$ should be approximately equivalent, so we localize the optimal CoR in the range of $[\xi_{min}, \xi_{max}]$ for the *i*th sinogram by formulating:

$$C_i^* = \min_c \frac{1}{N} \sum_j^N (r_c(\xi_j, \varphi_j) - r_c'(\xi_j, \varphi_j)) \quad (5)$$

For the selected ρ sinograms, the localized optimal CoRs are $C = \{C_1^*, C_2^*, \dots, C_\rho^*\}$; so the most frequently occurring value C^* in C is referred to as the CoR for a single channel, either the bright-field or fluorescence channel.

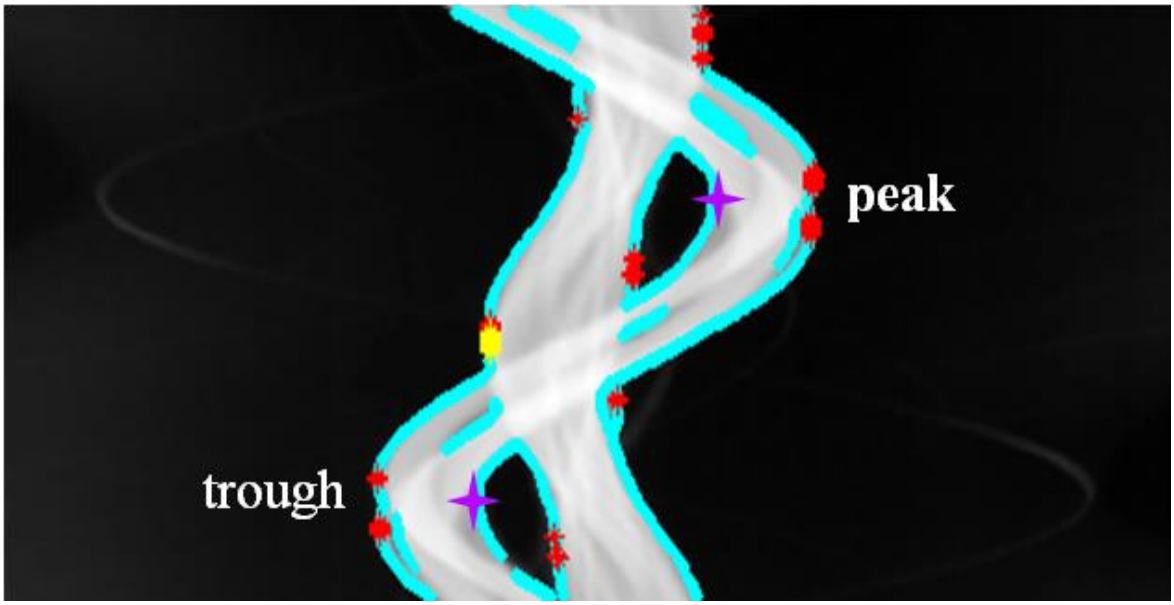

Figure 2.6. A bright-field sinogram (displayed inverted) from a chicken heart images with interest points detected (shown as red and yellow stars). Edge points, i.e. initial points, are shown in cyan; while false-peaks are shown as purple stars.

For multiple channels the sinograms should be aligned to the same size with the same CoR before 3D reconstruction. The disparity between different channels may be a result of a mechanic drift, when images are recorded at different time. We illustrate our alignment scheme in two channels (fluorescence and bright-field), but it is also suitable to multiple channels. The *i*th sinogram S_i of size $\phi \times p$ in each channel is aligned centered by C^* as S_i' of size $\phi \times q$. This is accomplished by using:

$$q = \begin{cases} 2 \times C^*, & C^* < \frac{p}{2} \\ 2 \times (p - C^*), & C^* \geq \frac{p}{2} \end{cases}, \tag{6}$$

and

$$S_i' = \begin{cases} S_i(1{:}\,2C^*, \varphi), & C^* < \frac{p}{2} \\ S_i(2C^* - p{:}\,p, \varphi), & C^* \geq \frac{p}{2} \end{cases} \tag{7}$$

As illustrated in Eq. (6), q is calculated to be smaller than p to preserve sufficient sinogram information, as well as to avoid redundant background reconstruction, i.e. S_i is truncated instead of being extended, which consumes more time for reconstructing the background. With Eq. (6) and Eq. (7), the *i*th sinogram for the fluorescence and bright-field channel are S'_{fi} and S'_{bi} with size of $\phi \times q_f$ and $\phi \times q_b$ respectively. They are aligned to the same CoR with the same size as S^*_{fi} and S^*_{bi} by using:

$$\begin{cases} S^*_{fi} = (z_0, S'_{fi}, z_0);\ S^*_{bi} = S'_{bi}, & q_f < q_b \\ S^*_{fi} = S'_{fi};\ S^*_{bi} = (z_0, S'_{bi}, z_0), & q_f > q_b \end{cases} \tag{8}$$

where z_0 is a Zero matrix with size of $\phi \times |C^*_f - C^*_b|$, and C^*_f and C^*_b represent the located CoRs for the fluorescence and bright-field channel.

2.3.2 Reconstruction and fusion

Next, from the corrected sinogram, now we have a new sinogram. Applying inverse radon transform or filtered back projection (FBP) [52] to both the bright-field and the fluorescence channel of the obtained samples, the reconstructed images are formed as $R_b^t = \{R_{b1}, \dots, R_{bl}, \dots, R_{bL}\}$ and $R_f^t = \{R_{f1}, \dots, R_{fl}, \dots, R_{fL}\}$ respectively. L is the number of sinogams at imaging time *t*. The intensities in R_{fl} and R_{bl} refer to the fluorescence and bright-field signals. For transparent specimens, such as the zebrafish larvae from our experiments, the bright-field signals are generally distributed in vertebra and cartilage, providing a description of the silhouette of the zebrafish. Therefore, by fusing R_f^t and R_b^t, fluorescence signals, for instance a pattern of gene expression could be located and analysed within specimens at the specific time t. R_f^t and R_b^t are fused according to their equivalent slice number l and imaging time *t*. For each voxel in the fused 4D image, $V_{(x,y,l,t)} = (I_f, I_b)$ describes its signals of different channels, and (x, y, l, t) symbolizes

the coordinate in 4D space. (x, y) corresponds to the pixel of the reconstructed image slice, while l and t symbolize the slice number and imaging time. $V_{(x,y,l,t)}$ could be further used in a 3D segmentation procedure and quantification of fluorescence, i.e. gene and/or protein activity, in the specific specimen or organs.

2.3.3 Parallel setting

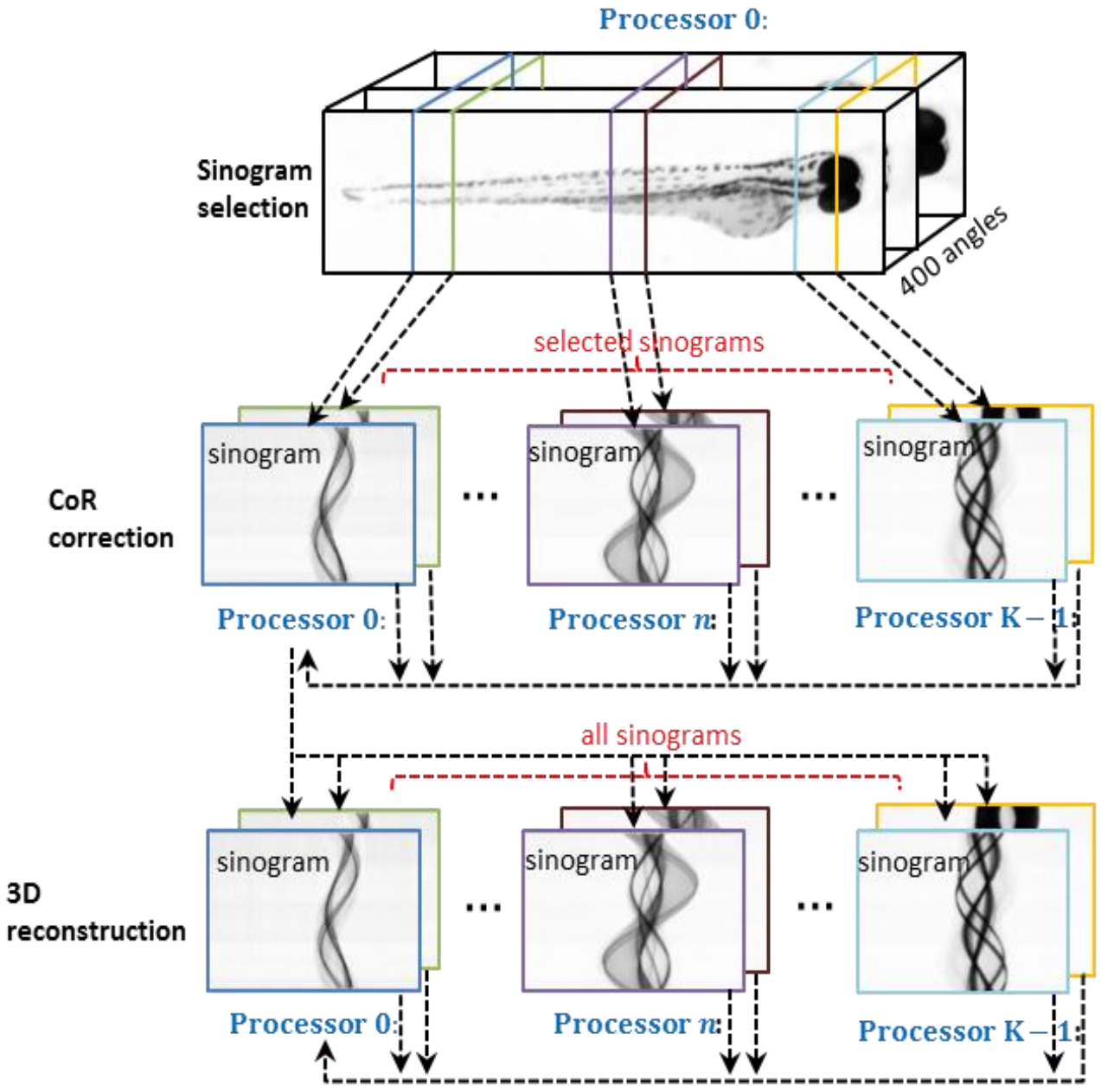

Figure 2.7. Parallel framework for CoR correction and 3D reconstruction. Processor 0 is responsible for sinogram selection, broadcast and collective communication, as well as normalization before image writing.

In order to speed up computations, we implemented a parallel computing scheme on our cluster computers, i.e. LLSC, for both the CoR correction as well as for the 3D reconstruction. This scheme is an essential part of our proposed pipeline. The specific implementation is illustrated in Figure 2.7. *K* represents the number of available processors. Processor 0 is defined as the Master processor unit responsible for sinogram selection, broadcast and collective communication. The selected sinograms *S* are then distributed to the *K* processors for localizing the corresponding CoRs using Eq. (5). All the CoRs from different processors are gathered by the Master processor unit to calculate the C^* of each channel. Subsequently, the CoR alignment of the different channels using Eq. (6), Eq. (7) and Eq. (8) is also processed on the Master processor unit. After CoR correction, the Master processor unit distributes the *L* slices of aligned sinograms to the *K* processors for the 3D reconstruction. The reconstructed image slices will be gathered again to the Master processor unit for normalization before image writting.

2.4 Experiments

In this section, we first evaluate the reconstruction pipeline without the CoR correction, qualitatively and quantitatively comparing the results with the pipeline considering the CoR correction. The runtimes of distributed computing for both experimental setups are measured and compared. We present a new CoR correction algorithm in this chapter, therefore further performance comparisons with previous CoR correction algorithm are also included.

2.4.1 Experiments on the fast post-processing pipeline

Instead of calibration of CoR based on adapting the adequate parts in the imaging system, we acquired a tomogram of a zebrafish sample and reconstructed it using the proposed pipeline. The raw 1036×1360×400 OPT tomogram was first cropped, producing a smaller image size of 506×1360×400, followed by a background subtraction from the 10 background images acquired, cf. § 2.2.2. The cropping and background subtraction normally take less than 1 second, the average time of each channel for CoR correction and 3D reconstruction is 15.05s and 18.81s respectively with 5 nodes of 8-core 2.66 GHz CPU+ 16G RAM and 8 nodes of 4-core 2.66 GHz CPU+16G RAM. The number of selected sinograms is set to $\rho = 40$ to balance the effectiveness and computational complexity of CoR localization, and the patch size is $w_1 = 15$. The visualizations of 3D reconstruction without and with the CoR correction are respectively shown in Figure 2.8 (a), (b), (c) and Figure 2.9 (a), (b), (c). It is obvious that Figure 2.9 (a), (b) and (c) contain distinct signals in both channels while Figure 2.8 (a), (b) and (c) show blurred 3D models and signals. Maximum projections of 10 slices of cross-section image selected from the combination model in (c) are magnified in Figure 2.8 (d) and Figure 2.9 (d). Figure 2.9 (d) accurately represented the zebrafish spinal cord and specific GFP fluorescent signals.

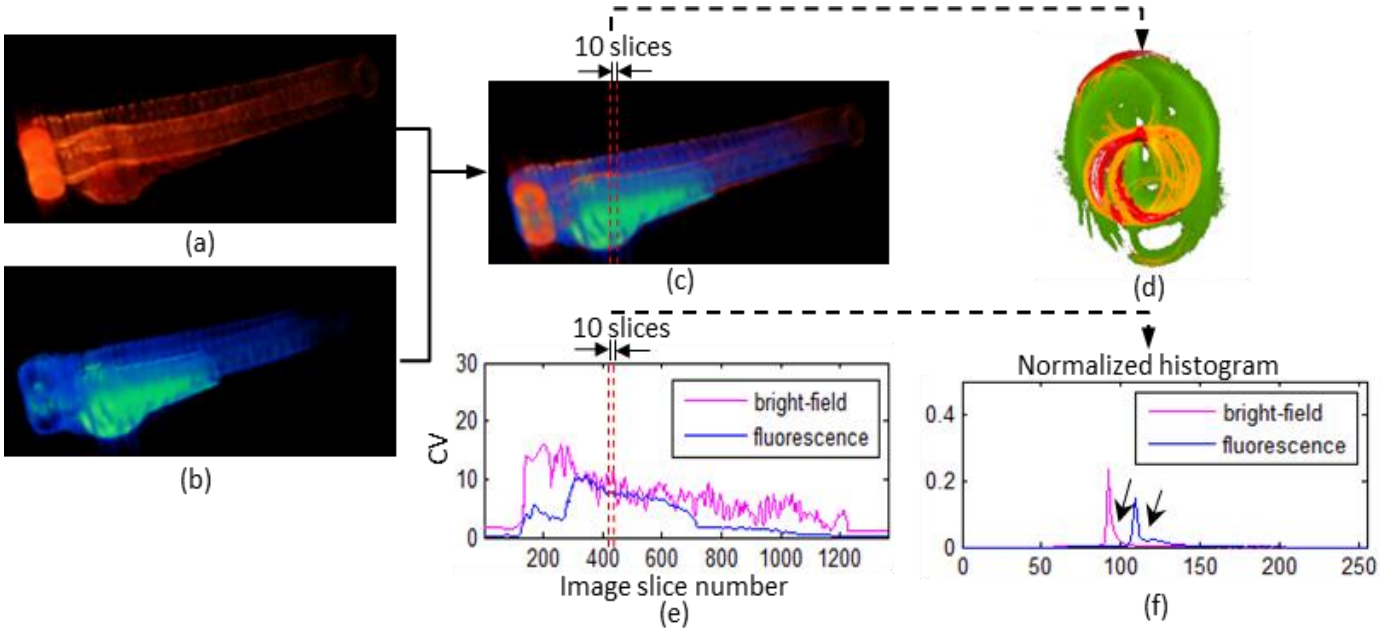

Figure 2.8. An example of 3D reconstruction for a zebrafish without CoR calibration prior to image acquisition . The results are obtained based on the proposed pipeline without CoR correction. (a) , (b) 3D image in bright-field and Fluorescence channel. (c) The combination of (a) and (b). (d) Reconstructed slices between 410 and 419 of (c). The bright-field and fluorescence signals are shown in red and green and the intersections of them are in yellow. (e) The coefficient of variation of all slices corresponding to (c). (f) Normalized histograms for the average of the 10 slices selected from (c) and (e) . black arrows indicate the statistical characteristics of the reconstructed silhouette for the zebrafish.

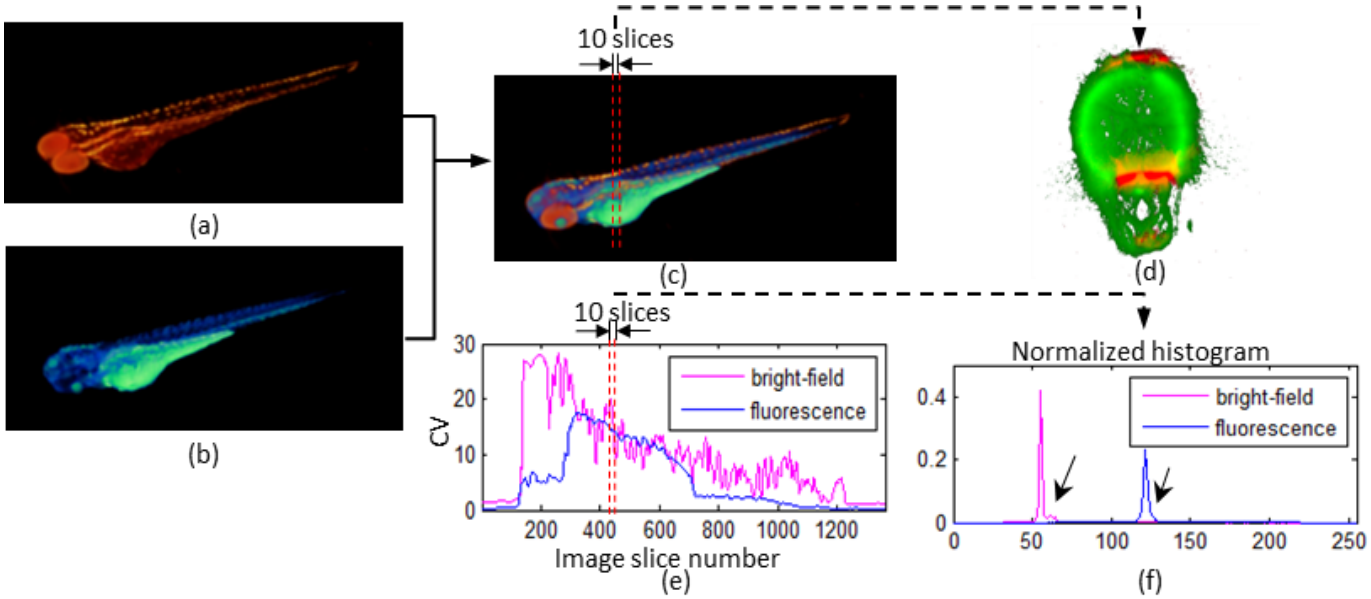

Figure 2.9. 3D reconstruction for the same zebrafish sample as Figure 2.8, without CoR calibration prior to image acquisition , but the omission of the calibration is compensated with the proposed pipeline with CoR correction. (a), (b) 3D image in bright-field and Fluorescence channel. (c) Combination of (a) and (b). (d) Reconstructed slices between 410 and 419 of (c). The bright-field signals (in red) show the outline of the zebrafish. The fluorescence signals (GFP) are

shown in green and the brightness of color indicates the strength of GFP signals, decribing the fluorescent texture. (e) coefficient of variation of all slices corresponding to (c). (f) Normalized histograms for the average of the 10 slices selected from (c) and (e). The peaks (background) are higher and the edges (black arrow) are much sharper compared to those in Figure 2.8 (f).

To quantitatively compare the difference between the reconstructed slices without and with CoR correction, coefficient of variation (CV): $\mathrm{CV} = \frac{\sigma}{\mu}$ is calculated for each reconstructed slice as shown Figure 2.8 (e) and Figure 2.9 (e). It should be noted that the CVs calculated in our experiments are based on the raw reconstruction without scaling. In terms of reducing artefacts produced in the reconstruction, we aim to simultaneously maximize the variance and minimize the mean of bright-field and fluorescence signals, presenting the specimen with the least of blur. By comparing Figure 2.8 (e) with Figure 2.9 (e), we can see that after CoR correction CV increases significantly on all slices in both channels.

To observe more details in the reconstructed image slices, the histograms for the average image of the selected 10 slices without and with CoR correction are illustrated in Figure 2.8 (f) and Figure 2.9 (f). The pixel value corresponds to the bright-field or fluorescence signal strength. In practice, the bright-field image is inverted to satisfy the correspondence of pixel value and signal strength. In Figure 2.8 (f) and Figure 2.9 (f), the peaks of the histogram indicate the pixel values of the background, and values for signals are on the right of the peak. We can observe that the background boundary of the histogram (black arrow) in Figure 2.9 (f) is sharper than that in Figure 2.8 (f). The peaks in Figure 2.9 (f) are both higher than peaks in Figure 2.8 (f), indicating that CoR correction clears the background which is smeared by blurred artefacts. This is consistent with the refined and distinct silhouette and texture of reconstructed image with CoR correction.

To illustrate the over-all runtime of the pipeline in our system, we repeat the experiments on 10 more sample specimens including zebrafish, zebra-finch embryo and adult chicken heart. These samples are acquired at different magnifications. The parameters for the CoR correction and the configuration of parallel computing are set as the same as the experiments above. The only difference is that we fixed the image size to the original 1036×1360×400 pixels without cropping to exclude the influence of different image sizes on the runtime. Figure 2.10 describes the runtime of 3D reconstruction (Rec) and that of 3D reconstruction with CoR correction (Rec&CoR). Over all, Rec takes an average time of 26.91s and Rec&CoR takes 54.66s for all the 10 dataset tested.

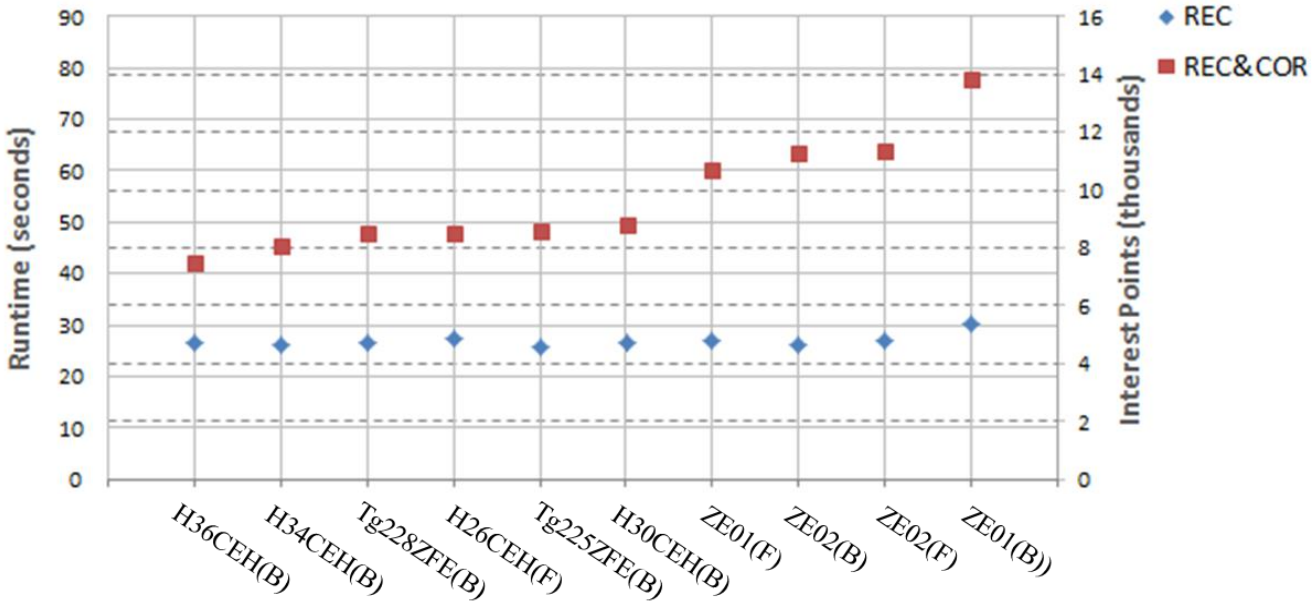

Figure 2.10. The runtime (solid axis) of the pipeline implemented on the cluster. Rec represents the runtime for 3D reconstruction and Rec&CoR indicates the runtime that includes CoR correction as well. The increasing runtime of REC&CoR corresponds to the increasing number of interest points (dashed axis) detected in the CoR correction algorithm on different data.

2.4.2 Comparison of different CoR corrections on different data

Three previous CoR correction approaches are analysed and compared to our method on the 12 OPT images. The Pixel Match method [42] and the Cross Correlation Operation (CCO) method [43] are based on signal match for pairs of projection, both of which are successfully used in CT CoR correction. The most commonly used method for CoR correction in OPT, as described in [46], here referred to as the Automated method. As the results of CoR correction depend on the selection of sinograms, the comparisons of different CoR correction methods are implemented on multiple sinograms selected with the proposed strategy above. For our experiments, the 12 OPT datasets consisting of whole-mount organisms as well as dissected organs. As the developmental stages differ, the size and shape differs. The samples comprise zebrafish embryo (ZE), chicken heart (CEH) and zebra finch embryo (ZFE) using both the bright-field (B) and fluorescence (F) channel. The samples are part of researches in embryo development, skeleton development and heart defection.

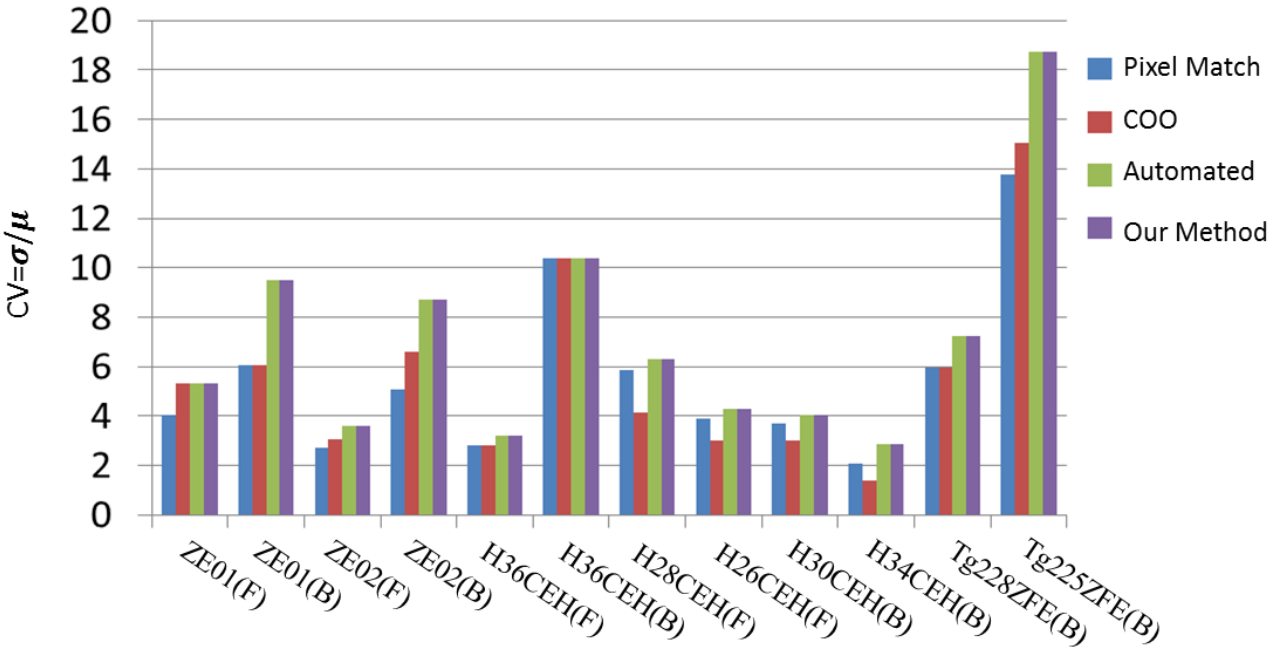

Figure 2.11. The comparison of average coefficient of variation (CV) for reconstruction with 4 different CoR correction methods on 12 datasets. For each dataset, larger CV corresponds to discrimination of information and less artefacts introduced by reconstrution. ZE: zebrafish embryo; CEH : chicken heart; ZFE: zebra finch embryo; Different prefixes refer to different developmental stages of the sample specimens at acquisition. B and F are the bright-field and fluorescence channel.

Table 2.1. Runtimes of different CoR alignment aprroaches in each sinogram on different datasets

Datasets	**Pixel Match**(s)	**CCO**(s)	**Automated**(s)	**Ours**(s)
ZE01(F)	0.6897	102.8966	1043.1034	10.3448
ZE01(B)	0.6765	102.7941	1042.7941	12.2941
ZE02(F)	0.6897	102.9310	1043.3793	11.7241
ZE02(B)	0.6786	102.8929	1042.8214	11.7241
H36CEH (F)	0.6774	102.9032	1043.2580	2.2258
H36 CEH (B)	0.6667	102.9333	1042.8444	6.2888
H28 CEH (F)	0.6800	103.1200	1043.1200	5.2000
H26 CEH (F)	0.7200	103.2000	1043.2000	4.3200
H30 CEH (B)	0.6774	103.5484	1043.1935	4.1612
H34 CEH (B)	0.6897	103.5517	1043.0344	3.3793
Tg228 ZFE (B)	0.7143	103.1786	1042.8571	2.6785
Tg225 ZFE (B)	0.7857	103.2143	1042.7857	2.7857
Average	**0.6955**	**103.097**	**1043.0326**	**6.4272**

In Figure 2.11 the results are depicted. These indicate the measurement of CV considering both the variance and mean of the reconstructed results, which are more convincing and reliable. The data used for CV calculation is the raw data after reconstruction but before image normalization, excluding the effect of scaling. We

should consider that the CV is only a criterion for evaluating the performance of different reconstruction of the same specimen. It is not suitable for comparing the reconstruction performance across specimens, because the variance and mean value differs in the different specimen structures. However for the same specimen, the CV is very suitable for evaluating reconstruction performance than variance in [46]. In Figure 2.11, the Automated method [46] and our method obtained maximum values for the CV in all the 12 datasets, because both methods achieved the optimal and equivalent CoR in each dataset. The Pixel Match [42] and CCO methods [43] gained different reconstruction and CV performance on the different data. The reason for this variation is that the algorithms in [42] and [43] strongly depend on the symmetry of all opposite projected pixel pairs. In the process of OPT imaging system, however, most of the pairs are not symmetrical.

Achieving competitive performance to the Automated method regarding to reconstruction quality in Figure 2.11, our method performs significantly superior to CCO method and Automated method in terms of its computational complexity; cf. Table 2.1. With the computer configuration of 16Gb RAM and 8-core 3.4GHz CPU, the average runtime of different CoR correction methods for single sinogram are 0.6955s, 103.097s, 1043.0326s and 6.4272s respectively. The Pixel Match method [42] achieves highest runtime performance, but its capability of optimal CoR correction is limited. Overall, our method outperforms the other three by considering the effectiveness and complexity of synchronous computation. It is noteworthy that in our method the runtime of different datasets varies due to the differences in the number of interest points. The other three approaches, however, consume approximately the same runtime for each sinogram because they are considering a fixed number of sinogram pixels.

2.5 Conclusions

In this chapter we presented a fast post-processing pipeline for OPT tomograms including cropping, background subtraction, CoR correction and 3D reconstruction, with focus on parallel computing. For CoR correction, a new automated CoR correction method was proposed, outperforming the other three CoR correction approaches in terms of general efficiency. In terms of 3D reconstruction, we have implemented the inverse radon transform on our cluster computer, i.e. LLSC, to achieve faster reconstruction. A pipeline was implemented using parallel computation and the average runtime based on the 10 datasets with a fixed image size of 1036×1360×400 is 54.66s, using 5 nodes of 8-core 2.66 GHz CPU+16G RAM and 8 nodes of 4-core 2.66 GHz CPU+16G RAM. Furthermore, the proposed CoR correction methodology could suppress random or fixed noise in background, because only peaks and troughs of the sinogram from foreground are detected as interest points. Importantly, the proposed pipeline and CoR correction are also suitable for 3D CT image reconstruction and comparison when used in medical therapy. Currently, the integrated system including imaging, data transfer, pre-processing, CoR correction, 3D reconstruction and visualization is being optimized as a distributed

application. With this integrated system, a profile of the organism/organ enhanced fluorescence probes within it can be imaged, reconstructed and visualized in a very short period of time. In our future work, a quantitative model for locating, calculating and tracking fluorescent signals (gene and/or protein activity) will be established.

2.6 Acknowledgement

The work is partially funded by China Scholarship Council (CSC). We would like to express our gratitude to Gerda Lamers and Merijn de Bakker (IBL, Leiden, Netherlands) for their supervision of the OPT preparation, Merel van't Hoff (LIACS, Leiden, Netherlands) and Monique Welten (currently: Naturalis Bio Diversity Center, Leiden, the Netherlands) for their contributions of sample preparation and imaging of the samples used in the experiments.